tvst

Article

Simulation of Vitreous Traction Force and Flow Rate of High Speed Dual-Pneumatic 7500 Cuts Per Minute Vitrectomy Probes

Paul J. Missel[1], Yongting Ma[1], Brian W. McDonell[2], Danial Shahmirzadi[1], Dina Joy K. Abulon[3], and Ramesh Sarangapani[1]

[1] Data Science and Digital Solutions, Alcon Vision, LLC, Fort Worth, TX, USA
[2] Surgical Instrumentation, Alcon Research, Ltd., Lake Forest, CA, USA
[3] Global Medical Affairs, Alcon Research, Ltd., Lake Forest, CA, USA

Correspondence: Paul J. Missel, Alcon Research, Ltd., TC-47, 6201 South Freeway, Fort Worth, TX 76134. e-mail: paul.missel@alcon.com

Received: February 28, 2019
Accepted: June 5, 2020
Published: July 30, 2020

Keywords: vitrectomy; retinal traction; modeling and simulation

Citation: Missel PJ, Ma Y, McDonell BW, Shahmirzadi D, Abulon DJK, Sarangapani R. Simulation of vitreous traction force and flow rate of high speed dual-pneumatic 7500 cuts per minute vitrectomy probes. Trans Vis Sci Tech. 2020;9(8):46, https://doi.org/10.1167/tvst.9.8.46

Purpose: To develop methods to simulate vitreous flow and traction during vitrectomy and qualify these methods using laboratory measurements.

Methods: Medium viscosity and phase treatment were adjusted to represent vitreous (Eulerian two-phase flow) or saline solution (single-phase Navier-Stokes flow). Retinal traction was approximated using a one-way fluid-structure interaction simulating cut vitreous volume coupled to a structural simulation of elastic stretching of a cylinder representing vitreous fibers entrained in the flow.

Results: Simulated saline solution flow decreased, but vitreous flow increased with increasing cut rate, consistent with experimental trends observed for the 50/50 duty cycle mode. Traction simulations reproduced all trends in variation of traction force with changes in conditions. Simulations reproduced the majority of traction measurements within experimental error.

Conclusions: A scientific basis is provided for understanding how flow and traction vary with operational parameters. This model-based analysis serves as a "virtual lab" to determine optimal system settings to maximize flow efficiency while reducing traction.

Translational Relevance: The model provides a better understanding regarding how instrument settings can help control a vitrectomy procedure so that it can be made as efficient as possible (maximizing the rate of vitreous removal) while at the same time being made as safe as possible (minimizing retinal traction).

Introduction

The objective of vitrectomy surgery is to remove the vitreous from a diseased eye without damaging the retina or other ocular tissues. This is challenging because vitreous material entering the vitrectomy probe can still be attached to the retina and may continue to exert force on the retina until it is cut. It may also be preferred to maximize the efficiency of vitreous removal by minimizing the time required for the procedure. To decrease this risk and improve the safety and efficiency of the procedure, the design of vitrectomy-based systems has advanced over time allowing the selection of smaller instruments with increased cutting speed and more flexible control of the duty cycle (the fraction of time in a cycle that the port is open).

Previous laboratory studies have been conducted to measure the fluidics[1–5] and traction forces[6–9] that might be exerted by these probes on ocular tissues. In this study, we present methods for simulating fluid flow through probes during simulated vitrectomy. Two different simulation methods are presented corresponding to the beginning and ending stages of the vitrectomy surgery, where the material being removed is comprised primarily of vitreous or saline solution, respectively. Results of flow simulations are compared

with bench measurements of porcine vitreous flow and saline solution for various probe gauges, cut rates, and duty cycles. A simple analytical method is proposed for calculating changes in flow behavior and fluid composition as the surgery progresses.

We present the first known computational model for simulating vitreoretinal traction exerted during a vitrectomy procedure. Measurements of traction during simulated vitrectomy were conducted using a recently developed laboratory procedure. During surgery, application of too much traction on the retina lead to retinal tear or detachment. In one study, Dogramaci et al.[10] reported the overall frequency of iatrogenic retinal breaks to be 10.09%. By providing a more in depth understanding of the effects with existing probes and operating conditions, this simulation tool can be used as a "virtual lab" to help in the design of improved vitrectors and operating procedures and thereby provide a rational basis for estimating and potentially improving the safety margin against iatrogenic retinal detachment and tears during clinical surgical procedures. It may also provide clinicians with additional insight into the physical mechanisms that govern how changes in instrument settings will affect retinal traction and material flow.

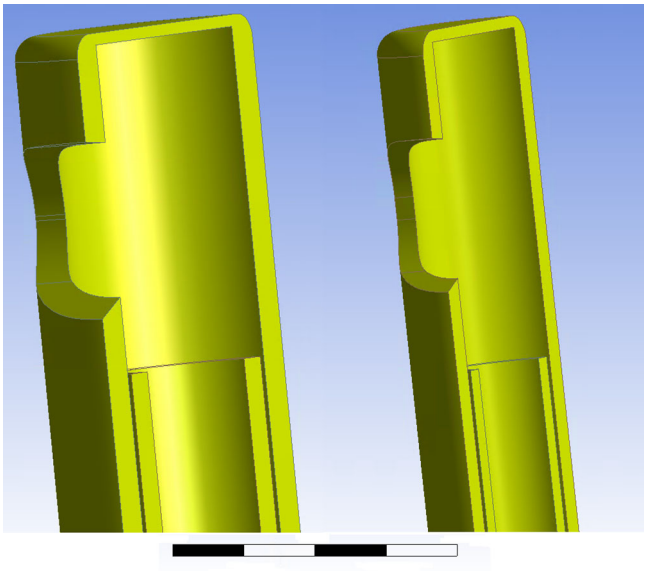

Figure 1. Close-ups of the ends of the cutting probes that were used in the study. Illustrations show half of each probe, with the inner shaft at the maximum open position. When cutting is engaged, the inner shaft moves toward the end of the probe to a position just past the most distal portion of the port opening and then returns to the starting location at the end of each cycle. *Left:* 23 gauge; *right:* 27+ gauge. Length of each bar segment in the ruler guide below is 0.15 mm (0.6 mm total length).

Methods

Performance of two different gauges of vitrectomy probes were simulated for use with the CONSTELLATION Vision System (Alcon, Geneva, Switzerland): (1) UltraVit 27+ 7500 cuts per minute (cpm) probes and (2) UltraVit 23-gauge 7500 cpm probes (see Fig. 1). Vitreous flow rates, flow rates of buffered aqueous saline solution (Alcon BSS), and vitreous traction performance tests were modeled and analyzed. Various duty cycle modes (core, 50/50, and shave) and cut rates (2500, 5000, and 7500) were evaluated.

Experimental Measurements of Shaft Motion

Computational fluid dynamic simulation procedures require replication of the exact geometry of the system. The motion of the inner shaft changes the geometric flow domain with time; therefore it was necessary to measure the time-varying configuration of the inner shaft, because it would be moving during surgical operation. Vitrectors were mounted in a jig that enabled the position of the inner shaft motion to be measured as a function of time using a laser system which allows the position of the inner shaft to be recorded over time. The vitrectors were then attached to a CONSTELLATION Vision System, which was used to drive the vitrectors at various cut rates and duty cycles. The position was recorded with a time resolution of 0.1 msec. It was assumed that the vitrector motion measured was comparable to the motion conducted during an actual surgery under identical instrument settings.

Experimental Measurements of Flow and Traction

The methods used for obtaining the flow rates of vitreous and buffer during the laboratory vitrector measurements have been described in the previous studies.[2–4] The measurements of vitreous traction were taken from the study of Abulon et al. (Abulon DJK, et al. IOVS 2016;57:ARVO E-Abstract 4462).

Computational Modeling Approach

The process by which a vitrector removes vitreous from an eye was modeled using the well-established one-way fluid-structure interaction scheme, in which the output from a fluidics simulation is provided as input into a structural mechanical simulation. The fluidic simulation models the time sequence of the flow of vitreous material into the vitrector, using a

computational fluid dynamic (CFD) analysis method. The result of this first simulation is provided as an input into a second completely separate and independent simulation, in which the finite element analysis (FEA) method is used to determine the corresponding time sequence of traction force applied by the vitreous fiber bundle on the retina as it is entrained in the aspiration flow into the cutter port. Each of these simulations is conducted by applying the physical laws of fluid flow (CFD) or the mechanics of structures (FEA) to well-defined geometric domains, determining the numerical solutions of equations subject to particular boundary conditions to represent the procedure and assigning certain properties to the materials as required by each method.

In developing these simulation methods, it is customary to begin using the simplest models for the geometric domain and the behavior of materials and applicable physical laws, and to determine how well these simpler models can reproduce the observed experimental results, before advancing to models that are more complex. In the methods described below, the assumptions made are specified. Our fluid simulation assumes Navier-Stokes flow; our structural simulation uses an isotropic elastic model for the vitreous fiber bundle. We have found that these relatively simple models are sufficient to reproduce the experimentally observed values. This is what is typically referred to as qualifying a model. If a simulation method can reasonably reproduce the experimental measurements for which it was designed to simulate, then it is considered qualified for the particular purpose in scope. The vitreous is a complex material having properties of both fluid and gel that change when cut by a vitrector (see for example reference 8). The physics of the situation was simplified by making the following assumptions. First, before the vitreous is cut, it is considered to behave as a purely elastic solid as it is drawn into the probe. It is presumed that it is the bundles of collagen fibers that are exerting the force on the vitreous. Once the portion of collagen fibers drawn into the probe is cut, it is separated from the portion outside the probe and will flow as a liquid as it is being aspirated through the inner shaft. To simulate the vitrector advancing toward the location of vitreoretinal adhesion three separate simulations for locations distal to, midway, and proximal to the location of vitreoretinal adhesion.

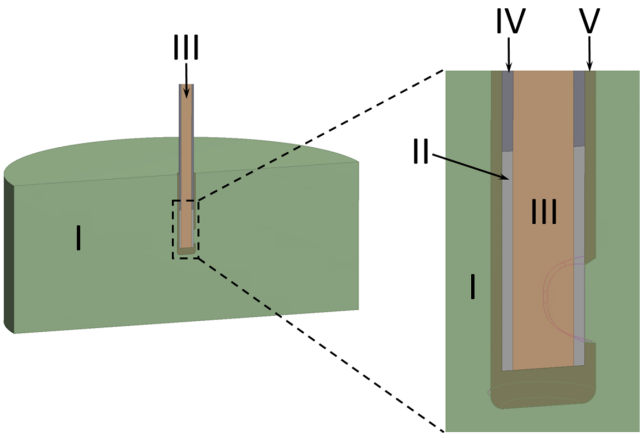

Figure 2. Geometric domain used for CFD simulations. The larger diameter cylindrical portion (*Region I*) is the uncut vitreous. The very narrow diameter cylindrical portion (*Region III*) is the fluid domain of the inner shaft and extends 44.5 mm from the bottom of the probe (not shown). *Region II* is the moving wall region enabling simulation of shaft motion. *Region IV* represents the inner shaft when it is in its highest (most open) position. *Region V* represents the outer shaft. Because no flow ever occurs in *regions IV* and *V*, they are excluded from the model.

Fluid Dynamics Model

The domain used for the fluid model was constructed in three dimensions with symmetric geometry as shown in Figure 2. The model represents a vitrector situated in a portion of the vitreous. This single geometry represents a simplification of all the possible configurations of a vitrector probe with respect to its orientation and approach to ocular tissue. Zone I represents a region of the vitreous near the vitrector tip. Our simulations used a cylindrical region 8 mm in diameter and 3.3 mm tall for Zone 1, as illustrated in Figure 2. The exact dimensions of Zone I are not important. For example, it was found that simulation results were unchanged even if the diameter of the cylindrical region were reduced to 0.6 mm. The vitrector was placed along the symmetry axis of Zone I and was positioned vertically such that the center of the port is at the mid height of the cylinder. The vitrector inner and outer shafts are represented by Zones IV and V, respectively. With the inner shaft raised to its highest position to open the port, the vitrector shaft geometries were subtracted from the domain. Zone II is a cylindrical shell zone with mesh motion corresponding to the movement of the inner shaft. During each simulated motion cycle, the height of this zone changes from the full extent shown to zero and then back to its original height with sinusoidal motion. Zone III is the inner hollow portion of the inner shaft, which extends 44.5 mm above the lower end of the shaft (only the lower portion of this zone is shown in the figure). Operational details for performing the transient CFD analyses are described in Appendix A.

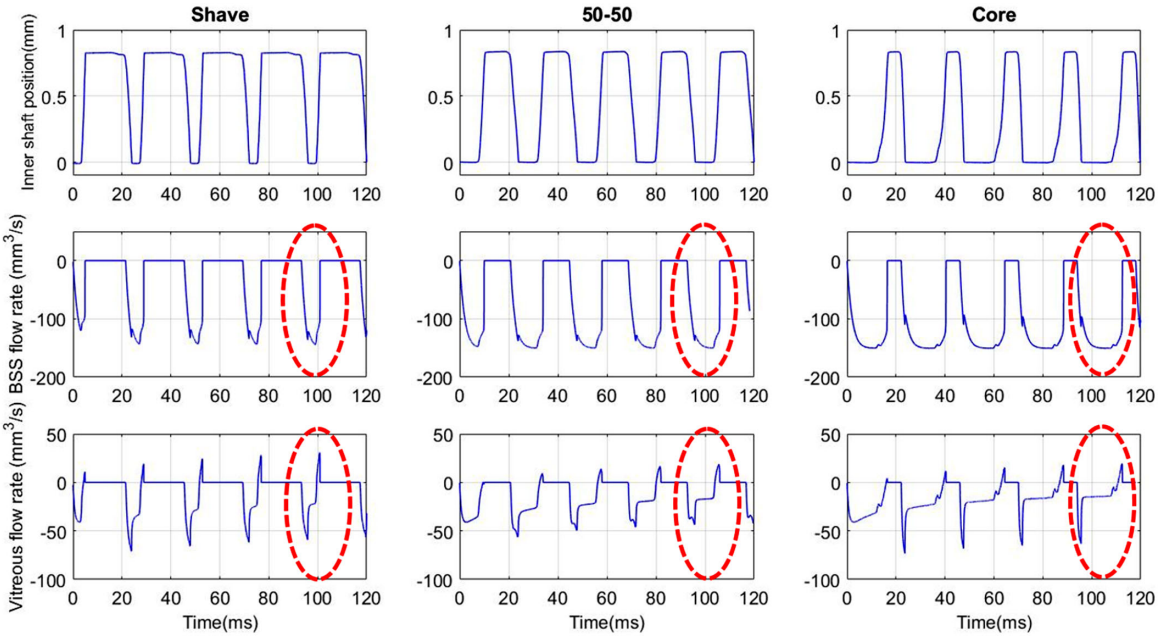

Figure 3. Input and output of fluidic simulation for 27+-gauge probe, 2500 cpm. *Upper panels:* Experimentally measured position of the inner shaft with time. A zero value corresponds to the inner shaft extended in the fully opened position. *Central panels:* Simulated volume flow rate of aqueous buffer through the vitrector (which represents half the total geometry). The *dashed circles* show the portions of each simulation (the fifth cycle of shaft motion) that was used after the system came to quasi-steady-state equilibrium. *Lower panels:* Simulated vitreous volume flow rate through the vitrector. The *dashed circles* show the portions of each simulation (the fifth cycle of shaft motion) that was used to drive the corresponding structural simulation.

Structural FEA Model

The geometric domain for the structural model was a narrow cylinder corresponding to a bundle representing an ensemble of all the vitreous fibers entrained in the flow into the cutter. This is a simplification of the actual geometry of a fiber bundle within the vitreous, which will most likely have a very complex shape before it is drawn into the vitrector. Simulations were conducted for cylinders of length 10, 25, and 50 mm, representing various stages of the vitrector procedure in the test method. A fixed support boundary condition is applied to one end of the cylinder, representing the attachment of the vitreous sample to the retina. A time-varying displacement boundary condition is applied to the other end of the cylinder, representing where the vitreous bundle is being drawn into the vitrector from the flow of cut vitreous fluid. The vitreous bundle is attributed to have linear elastic properties. To provide estimates for mechanical properties of vitreous fibers, we cannot rely on studies that measure rheological properties of the bulk material (see for example reference 11). Instead, we use properties based on measurements of a variety of biomaterials comprised of hydrated collagen fibrils (see discussion). We assume a shear modulus of 3 MPa and a Poisson's ratio of 0.45. The corresponding values of the Young's and bulk moduli for an isotropic material are 8.7 and 29 MPa, respectively.[11] The diameter of this representative bundle was adjusted to provide agreement between the traction force measured experimentally and simulated for one set of conditions (cutter gauge, cut rate and duty cycle) and was used for all subsequent conditions. The diameter of this representative bundle was 0.085 mm. The length of the bundle was set to the distance between the cutter port and the force sensor to which the vitreous sample was attached. Details for performing the transient structural simulations appear in Appendix B.

Results

Fluid Dynamics of the Ultravit Device

Figure 3 shows the experimentally measured position profiles for the inner shaft of a 27+-gauge probe operating at 2500 cpm for each of the Shave, 50-50 and Core duty cycles (upper panels). A zero value corresponds to the inner shaft extended to the fully open the port. The corresponding simulated volume flow rates for aqueous buffer and vitreous

obtained for each duty cycle position profile appear in the corresponding central and lower panels. There are variations in flow as the inner cutter transitions through different phases of the cut cycle. A negative volume flow rate is associated with removal of material from the system. Thus, when the port is fully open, the aqueous flow becomes negative, and when it is closed, the flow drops to zero. The flow of vitreous follows the same general pattern, but exhibits a more complicated pattern for reasons that will become apparent below. The portions of the volume flow curves circled were used to calculate the integrated volume flow, which for the vitreous were used to drive the structural simulations. This portion of these curves for the 50-50 duty cycle are expanded in the upper panels of Figures 4a and 4b, which are divided into different stages of an individual cutting cycle.

The lower panel of Figure 4a shows the integration of the vitreous flow in the upper panel to yield the accumulated vitreous flow volume during the cycle. When the shaft is in the lowest position, the port is closed, there is no flow, and both the volume flow rate and accumulated volume flow are zero (Stage I). As the inner shaft moves upward (Stage II), the port opens and a strong negative flow rate is quickly established and is comprised of two contributions: simple aspiration from the suction pressure applied at the base of the inner cutter (inside the probe), and an additional contribution as fluid rushes in to fill the void created by the upward displacement of the shaft. When the shaft is stationary at its uppermost position (Stage III), aspiration is driven only by the suction pressure boundary condition, and there is a noticeable decrease in slope in the accumulated volume flow. When the shaft is moving downward (Stage IV), the aspiration by suction is temporarily reduced by the opposing displacement of fluid by the inner shaft (retropulsion), and there is a slight decrease in the accumulated volume outflow. At stage V, the collagen fiber is cut.

Figure 4b shows the analysis of the flow simulation for aqueous solution and the integration of accumulated aqueous flow during the cycle, similar to the vitreous. The flow rate for aqueous solution is always negative. The integrated volume flow curve for aqueous fluid is much simpler than for vitreous, approximating a simple linear curve during the portion of time that the port is open.

The upper panels of Figure 5 show the displacement profiles used to drive the structural simulations, obtained by applying the equation in the methods section to the integrated volume flow profiles obtained in the fluid simulations for each respective duty cycle. Note that Stage V corresponds to Stage I (the port fully closed) of the succeeding cycle and was omitted

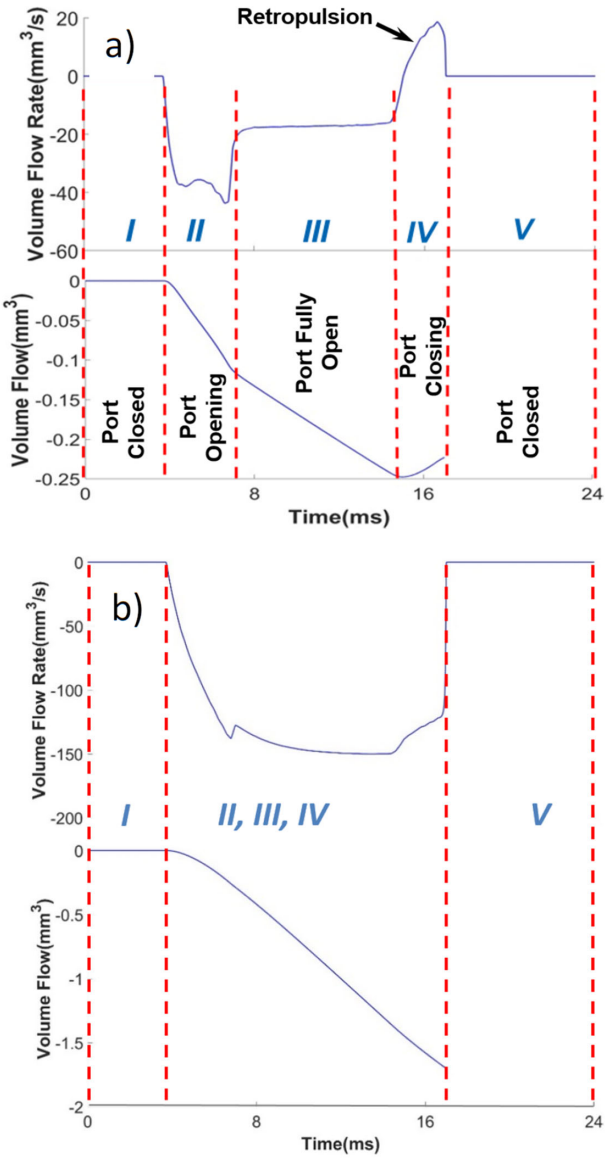

Figure 4. Analysis of flow simulations. a) Analysis of vitreous flow. *Upper panel:* enlargement of volume flow rate from fifth cycle of flow simulation for the 50-50 duty cycle of Figure 3. *Lower panel:* integration of upper panel to show accumulation of flow over time. Roman numerals indicate the various stages of a cut cycle as follows. *Stage I:* Port fully closed, inner shaft at bottom, no aspiration. *Stage II:* Port opening, inner shaft moving upward. *Stage III:* Port fully opened, inner shaft stationary. *Stage IV:* Port closing, inner shaft moving downward. *Stage V:* Collagen fiber cut. Note that this last stage is not considered in the displacement condition applied in the structural simulation because the fiber is presumed to have been cut at the end of Stage IV. b) Analysis of flow of buffer. Annotations similar to those for the vitreous. *Upper panel:* volume flow rate for the same duty cycle as for the vitreous. *Lower panel:* integration of the upper panel to show accumulation of flow over time. Roman numerals indicate the same stages of the cut cycle as for the vitreous.

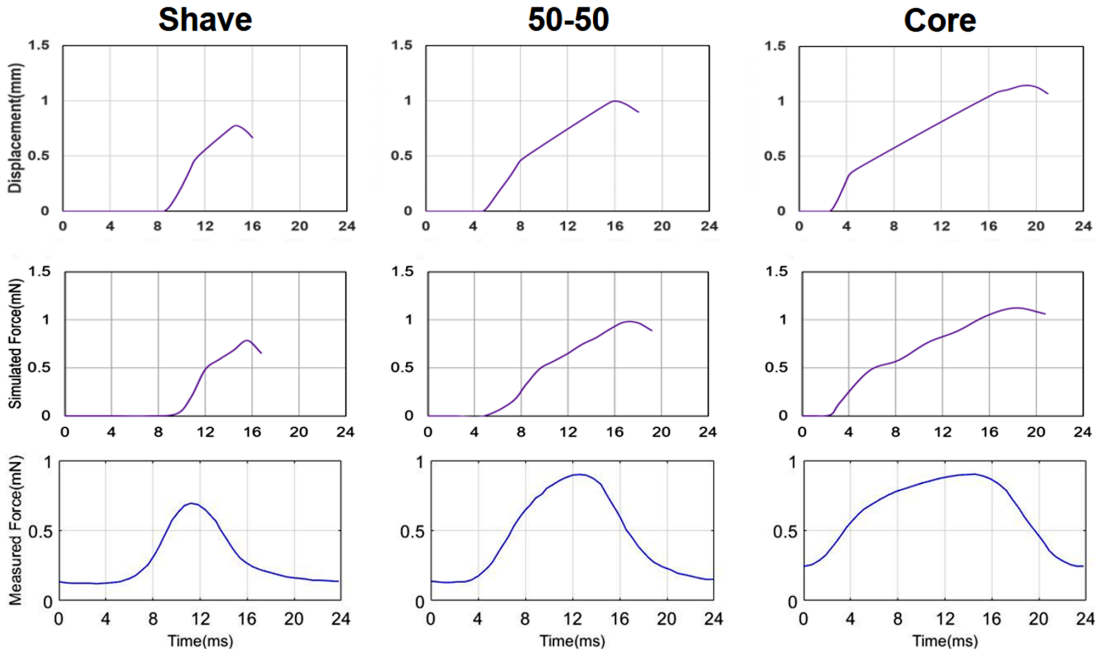

Figure 5. Comparison of FEA simulation results and experimental tractional force measurements. *Upper panels:* displacement obtained by applying equation for d(t) to the volume flow simulations for the 27+ gauge probe. *Central and lower panels:* Simulated and experimentally measured traction force over time for each corresponding duty cycle.

from the displacement profile inputs into the structural simulations. The central panels of Figure 5 show the simulated traction force, and the lower panel shows the experimentally measured traction profile for the corresponding duty cycles. The simulated force profiles end when the port is fully closed, because the vitreous bundle has been cut at this point in the cycle. The changes in slope for the various stages of the cutting cycle are apparent in both the simulated and measured traction force profiles.

Qualification of Flow Simulation

Comparisons of experimentally measured and simulated aqueous solution and vitreous flow rates appear in Figure 6. Experimental flow rates were taken from previous studies.[2,3] The vacuum for 27+-gauge probes was 650 mm Hg for both simulated and experimental results. The simulated vacuum for 23-gauge probes was 300 mm Hg. This is lower than the 450 mm Hg setting engaged during experimental measurements for flow rate with 23-gauge probes. This lower value was used in our simulations to match the experimental gauge setting for 23-gauge probes in bench experiments for vitreous traction.

Figures 6a and 6b compare the influence of cut rate at 50/50 duty cycle for the 27+-gauge and 23-gauge probes, respectively; Figures 6c and 6d compare the influence of duty cycle at a cut rate of 2500 cpm for the two gauge probes.

The following general trends were observed in the flow rate simulations. At a given gauge and 50/50 duty cycle, as cut rate increases, the flow rate for aqueous solution decreases, but the flow rate for vitreous increases (Figs. 6A and 6B). At a given gauge and 2500 cpm cut rate, flow rates for both vitreous and aqueous solution increases as the duty cycle changes from bias closed to bias open settings (Figs. 6C and 6D). These general trends are exhibited by the experimental data.[4] The simulations of aqueous buffer flow rates are within about 10% of the experimental measurements, although in many instances simulations fall beyond one standard deviation away from corresponding measurements. For vitreous flow rates, in most cases the simulated flow rates are in agreement with the measured flow rates within the range of experimental error, with three instances of overestimation by the simulations.

Qualification of Traction Simulation

Comparisons of previously reported experimental and simulation traction forces are presented in the tables. In Tables 1 through 4, both the peak force and

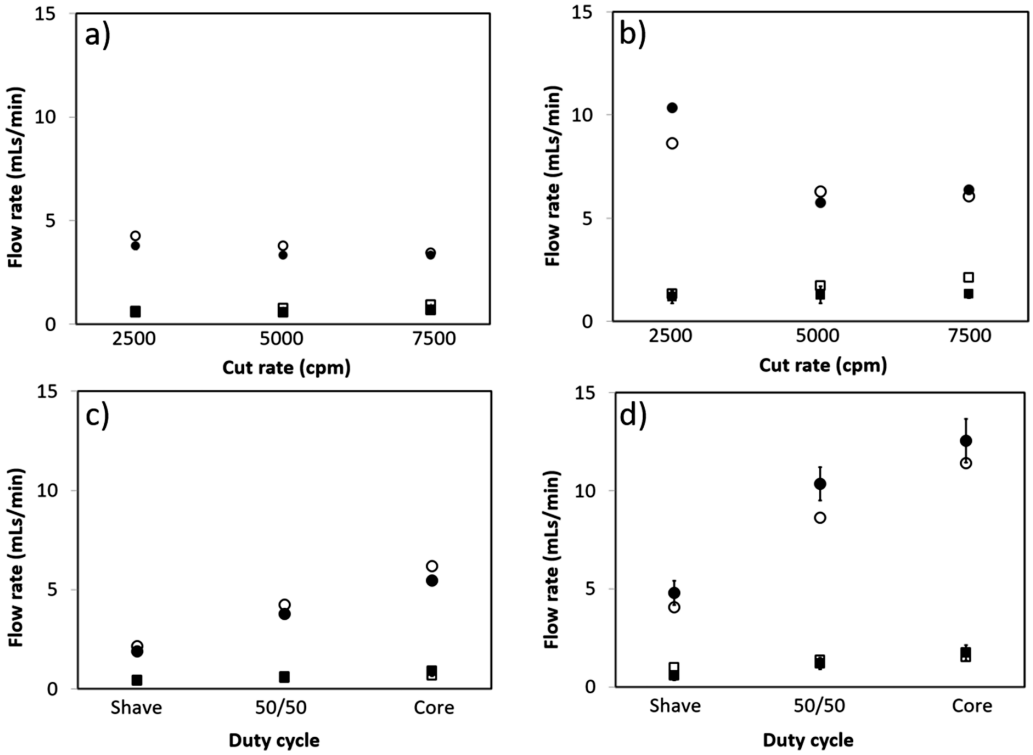

Figure 6. Comparison of simulated and experimentally measured flow rates. *Circles:* BSS flow rates. *Squares:* vitreous flow rates. *Filled symbols/solid trend lines:* experimental measurements. *Open symbols/dashed trend lines:* simulations. a) Influence of cut rate for 27+-gauge cutter, 50/50 duty cycle. All experiments and simulations conducted using 650 mm Hg aspiration setting. b) Influence of cut rate for 23-gauge cutter, 50/50 duty cycle. Experiments were conducted at 450 mm Hg, simulations at 300 mm Hg. c) Influence of duty cycle for 27+-gauge cutter, 2500 cpm cut rate. All experiments and simulations conducted using 650 mm Hg aspiration setting. d) Influence of duty cycle for 23-gauge cutter, 2500 cpm cut rate. Experiments were conducted at 450 mm Hg, simulations at 300 mm Hg.

Table 1. Comparison of Simulated and Experimental Vitreous Traction Force Data: Effect of Cut Rate, 27+ Gauge 50/50 Duty Cycle

	Peak Force		Mean Force	
Cut Rate (cpm)	Experiment (Mean ± SD)	Simulation	Experiment (Mean ± SD)	Simulation
2.5K	0.976 ± 0.224	0.976	0.427 ± 0.106	0.355
5.0K	0.734 ± 0.154	0.742	0.413 ± 0.089	0.274*
7.5K	0.558 ± 0.162	0.602	0.395 ± 0.089	0.232*

All force data are reported in mN.
*Below range.

the mean force (averaged using the trapezoidal rule over a single cycle) are reported. Tables 1 and 2 compare the effect of cut rate at the 50/50 duty cycle for 27+-gauge and 23-gauge probes, respectively; Tables 3 and 4 show the effect of duty cycle at a cut rate of 2500 cpm for the two probes. In most cases, the simulated peak and mean traction forces are in agreement with the experimentally measured forces within experimental error. In five instances, the simulated forces were slightly above or below the experimental range as indicated.

Tables 5 and 6 show the effect of distance from the force sensor on the mean traction force for 27+-gauge probes operating at the 50/50 duty cycle for 2500 and 7500 cpm, respectively. All measurements were within the experimental range, except for one, which fell below range.

Table 2. Comparison of Simulated and Experimental Vitreous Traction Force Data: Effect of Cut Rate, 23 Gauge 50/50 Duty Cycle

	Peak Force		Mean Force	
Cut Rate (cpm)	Experiment (Mean ± SD)	Simulation	Experiment (Mean ± SD)	Simulation
2.5K	1.100 ± 0.225	1.162	0.483 ± 0.106	0.529
5.0K	0.821 ± 0.161	0.778	0.459 ± 0.100	0.341*
7.5K	0.445 ± 0.161	0.663†	0.321 ± 0.119	0.317

All force data are reported in mN.
*Below range.
†Above range.

Table 3. Comparison of Simulated and Experimental Vitreous Traction Force Data: Effect of Duty Cycle, 27+ Gauge Cut Rate 2500 cpm

	Peak Force		Mean Force	
Duty Cycle	Experiment (Mean ± SD)	Simulation	Experiment (Mean ± SD)	Simulation
Shave	0.835 ± 0.308	0.782	0.319 ± 0.169	0.154
50/50	0.976 ± 0.224	0.976	0.427 ± 0.106	0.355
Core	1.091 ± 0.247	1.122	0.585 ± 0.150	0.571

All force data are reported in mN.

Table 4. Comparison of Simulated and Experimental Vitreous Traction Force Data: Effect of Duty Cycle, 23 Gauge Cut Rate 2500 cpm

	Peak Force		Mean Force	
Duty Cycle	Experiment (Mean ± SD)	Simulation	Experiment (Mean ± SD)	Simulation
Shave	0.629 ± 0.167	0.885*	0.230 ± 0.074	0.222
50/50	1.100 ± 0.225	1.162	0.483 ± 0.106	0.529
Core	1.348 ± 0.245	1.343	0.810 ± 0.159	0.742

All force data are reported in mN.
*Above range.

Table 5. Comparison of Simulated and Experimental Vitreous Traction Force Data: Effect of Distance From the Force Sensor, 27+ Gauge Cut Rate 2.5K cpm 50/50 Duty Cycle

	Peak Force	
Probe Distance Force Sensor	Experiment (Mean ± SD)	Simulation
Distal (50 mm)	0.976 ± 0.224	0.976
Midway (25 mm)	2.442 ± 0.902	1.965
Proximal (10 mm)	5.046 ± 1.383	4.907

All force data are reported in mN.

Table 6. Comparison of Simulated and Experimental Vitreous Traction Force Data: Effect of Distance From the Force Sensor, 27+ Gauge Cut Rate 7500 cpm 50/50 Duty Cycle

	Peak Force	
Probe Distance from Force Sensor	Experiment (Mean ± SD)	Simulation
Distal (50 mm)	0.558 ± 0.162	0.602
Midway (25 mm)	1.664 ± 0.741	1.162
Proximal (10 mm)	4.336 ± 1.068	2.866*

All force data are reported in mN.
*Below range.

Table 7. Influence of Duty Cycle, Cut Rate, and Vitrector Gauge on Vitrectomy Efficiency (Time in Minutes Estimated for 80% Vitreous Removal With Continuous Vitrector Engagement)

Duty Cycle	Cut Rate (cpm)	27+ Gauge	23 Gauge
50/50	2500	10.7	4.6
50/50	5000	8.7	4.0
50/50	7500	7.6	3.4
Shave	2500	16.0	7.0
50/50	2500	10.7	4.6
Core	2500	8.6	3.9

Simulations reflect similar trends observed experimentally and support previous mechanistic explanations for the observed effects:

- At a given duty cycle, vitreous traction force decreases as cut rate increases (Tables 1 and 2). This occurs because at higher cut rate the port is open for a shorter period of time, reducing the length of vitreous bundles drawn in before cutting releases the traction.
- At a given cut rate (2500 cpm), traction force increases as duty cycle varies from shave to 50/50 to core (Tables 3 and 4). This occurs because the length of vitreous bundles drawn in by aspiration suction before traction is released by cutting increases as the port open time increases.
- At a given cut rate and duty cycle, the traction force increases as the cutter advances closer to the point of attachment of the vitreous to the retina (Tables 5 and 6). This occurs because the length of vitreous bundles drawn in by aspiration suction before traction is released by cutting remains the same. This length constitutes a larger fraction of the total length of vitreous fiber bundles as the distance between the cutter and the force sensor decreases.
- At a given cut rate, BSS flow rate appears to increase as duty cycle varies from shave to 50/50 to core (Figs. 6c and 6d). This occurs because the fraction of time the port is open increases as the duty cycle varies from shave to 50/50 to core.

Comparison of Procedure Efficiency

The simulated flow rates can be used to compare the relative efficiency of each of the vitrector probes and operating conditions in removing vitreous, by comparing the rate at which vitreous material is removed during a vitrectomy procedure. At the beginning of a vitrectomy procedure, the eye is filled entirely with vitreous, whereas near the end of the procedure the eye is filled mainly with buffered saline solution. Rather than conduct a series of CFD simulations in which the fluid properties change continuously between these two extremes, a simple analytical relationship is derived in Appendix C to interpolate between the simulations conducted for the two extreme conditions representing the conditions at the beginning and at the end to provide an approximation regarding how the vitreous removal efficiency changes over time. Figure 7 shows how vitrector gauge, cut rate, and duty cycle influence the time dependence of the removal of vitreous fluid and buffer from the eye with time, using this simplistic analytical relationship. The procedure assumes that the cutters are engaged continuously, and that the buffered saline solution being infused to replace the aspirated fluid mixes uniformly with the contents of the vitreous.

In the plots showing vitreous fluid removed over time (left column of plots), a horizontal dashed line has been drawn at 4 mL. The time at which each of the curves crosses this line is compared in Table 6. From the table the following trends are shown:

- For each gauge probe, with a duty cycle of 50/50, increasing the cut rate from 2500 to 7500 cpm reduces the time for vitreous removal by about 30%.
- For each gauge probe, at a fixed cut rate of 2500 cpm, increasing the duty cycle from shave to core reduces the time for vitreous removal by almost half.

Discussion

It is important for the surgeon to understand how instrument settings can help control a vitrectomy procedure so that it can be made as efficient as possible, i.e., maximizing the rate of vitreous removal, while at the same time being made as safe as possible, i.e., minimizing retinal traction to potentially reduce iatrogenic retinal detachments or breaks.[12] Although it has been generally understood that vitreous traction is reduced as cutting rate increases,[13] it is important to appreciate how instrument settings can influence the flow of vitreous. To this end, modeling and simulation have been used to construct a virtual laboratory in which a model vitrector has been put through the operating conditions that correspond to various stages of a vitrectomy procedure. This exercise further supports existing explanations for vitreous traction and influence of parameters such as vitrector gauge, cut rate, and duty cycle on fluid removal and traction.

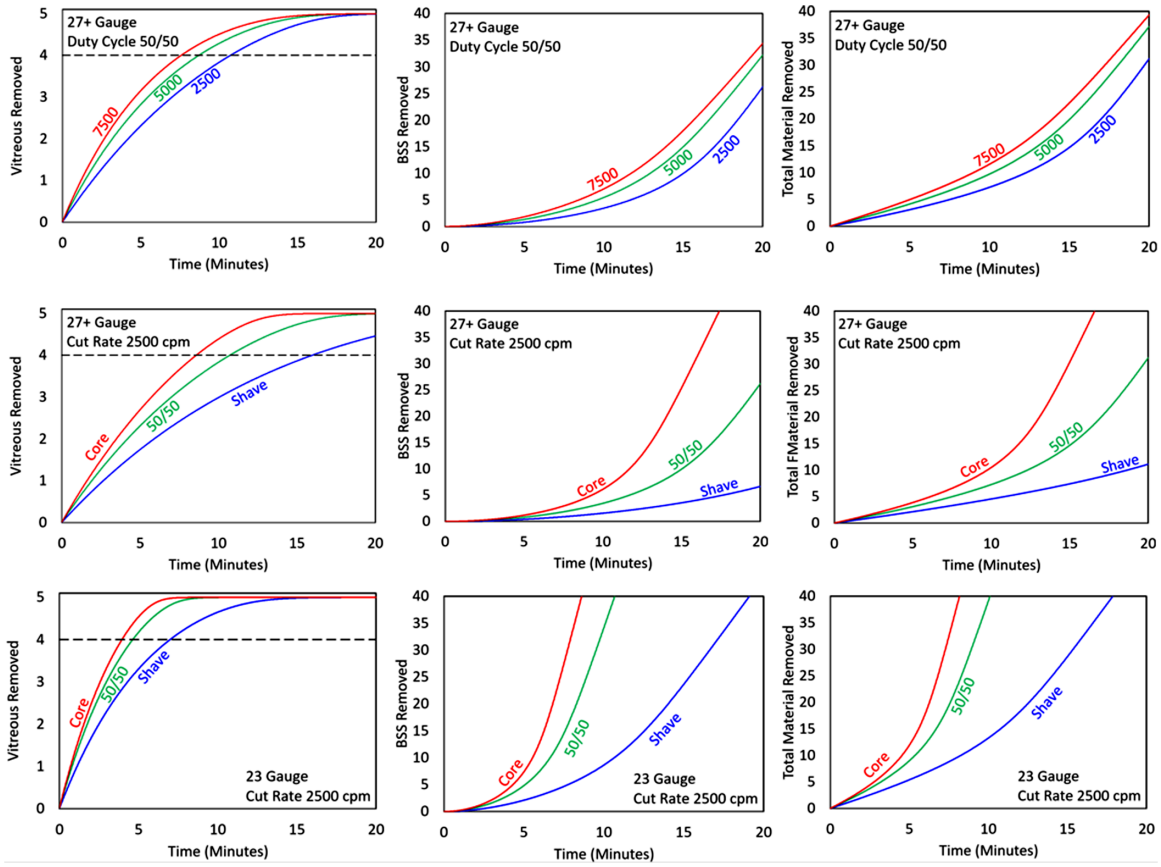

Figure 7. Comparison of progression of fluid removal during simulated vitrectomy procedures using various vitrector gauges, cutting rates, and duty cycles as labeled, calculated using the analytical functions in Appendix C. *Left panels:* removal of vitreous fluid with time. *Central panels:* removal of buffered saline solution. *Right panels:* total fluid removed. *Top row:* effect of cut rate for 27+-gauge vitrectors operated at 50/50 duty cycle. *Central row:* effect of duty cycle for 27+-gauge vitrectors operated at a cut rate of 2500 cpm. *Bottom row:* effect of duty cycle for 23-gauge vitrectors operated at a cut rate of 2500 cpm. Calculations presume that vitrectors are engaged continuously. Plots for the effect of cut rate for 23-gauge vitrectors are omitted but look similar to the plots in the first row.

Better understanding of how the vitrector works under various settings should help the operator anticipate what effects various settings have and enable them to make proper adjustments to better accomplish the task at hand, thus optimizing the use of the system and potentially improving the outcome for the patient.

The model behavior is consistent with the way surgeons may typically adjust instrument settings when the operation comes close to the retina. Setting adjustments can include the following:

- Reduce suction. Because traction is proportional to the length of vitreous fiber entrained into the vitrector before it is cut, traction force can be reduced by reducing the vitreous flow rate, which can be accomplished by reducing the suction pressure, because according to Poiseuille's law, the rate of flow through a tube is proportional to pressure. This can be especially important during the portion of the procedure in which the probe moves toward the periphery. Conversely, during the initial portion of the procedure when the probe is central and further away from the retina, the higher suction can allow for more rapid removal of vitreous.
- Increase cut rate. At fixed gauge and duty cycle, increasing cutting rate decreases the flow rate for pure buffered saline but has the opposite effect on the flow rate of pure vitreous. Although the amount of vitreous material aspirated while the port is open is less at higher cut rate, during a given time period, more aspiration/cutting cycles would occur at higher cut rate. The net effect is that during the same period of time, more vitreous fluid would be removed at a higher cut rate.

In the vitreous flow simulations, it was somewhat unexpected that the inner shaft motion temporarily

amplified or defeated the aspiration of vitreous when it is drawn inward (Stage II of Fig. 4) or pushed outward (Stage IV). In Stage IV, simulations predict the displacement of fluid by outward motion of the inner shaft temporarily outweigh inward flow by aspiration (retropulsion). This effect in vitreous may be seen in the faint fluttering motion of detached retina near the vitrector port. Simulations of flow of aqueous solution do not show this fluttering effect. The opposite effect is observed in Stage II. As the port opens, the shaft motion temporarily enhances aspiration. This is confirmed by the shape of the experimental traction force versus time profile, which exhibits two different slopes during the first half of the cycle.

An article evaluating instantaneous flow measurements reported similar findings of retropulsion. The fluctuating flow rate interfered with suction and hampered steady flow. The design of an ideal cutter would eliminate this fluctuation, eliminate changes in flow velocity during a cut cycle, eliminate acceleration, and ultimately eliminate traction forces applied to the retina.[14] Rossi et al.[14] emphasized that stable aspiration is desired to avoid inadvertent retinal entrapment, especially when working near a detached retina.

The simplified analytical approach in Appendix C serves as a crude but useful way of comparing how different vitrectomy probes and operating parameters will influence how the vitreous evacuation will proceed during a vitrectomy procedure. Because the aspiration is usually not applied continuously throughout the entire procedure, the analytical curves of Figure 7 most likely represent significant underestimates of the actual time that would be required to complete an actual surgical vitrectomy.

Furthermore, the incoming BSS fluid does not mix uniformly with the vitreous material yet to be removed from the vitreous, as was assumed by the analytical calculations. Additionally, during vitrectomy, the surgical environment is constantly changing and vitreous aspiration can vary between vitreous, aqueous solution, air, oil, membranes, and lens material (reference 12). Nevertheless, the approach provides a convenient way of comparing the efficiency of the various situations. Although an increase in efficiency of fluid removal may not amount to a significant reduction in the overall time of a vitrectomy procedure, more efficient vitreous removal may reduce instrument time.

In selecting the material properties for vitreous collagen fibers to use in structural simulations, we use measurements for other biomaterials comprised of hydrated collagen fibrils as we cannot rely on studies that measure rheological properties of the bulk material.[15] Using atomic force microscopy, Yang et al.[16] measured the shear modulus of fibrils isolated from bovine Achilles tendon equilibrated in buffered saline solution to be 2.9 $\pm$ 0.3 MPa, which corresponds to a Young's modulus of 8.4 MPa for a Poisson's ratio of 0.45. The value of 0.45 for Poisson's ratio is within the range of 0.45 to 0.49 typically used for soft tissues.[17,18] The mean value of the elastic slope for full-thickness human femoral cartilage samples cut perpendicular to the cleavage pattern reported by Silver et al.[19] was 10.5 $\pm$ 4.0 MPa. The transverse and longitudinal moduli for the axillary pouch of human glenohumoral capsule were reported by Moore et al.[20] to be 5.4 $\pm$ 2.9 and 14.8 $\pm$ 13.1 MPa, respectively. The value of Young's modulus that was used (8.7 MPa) falls within the approximate range of these measurements.

The distances over which the vitreous traction force was measured in the experimental method is larger than the dimension of a typical eye. In the measurement method, the vitreous sample is not contained within an eye but is suspended in saline solution, constrained only by its attachment at one point to a force sensor. When the vitrector aspiration and reciprocal shaft motion are engaged, the vitreous sample elongates toward the approaching vitrector, and the sensor detects a measurable force when the vitrector is more than 50 mm away.

These results confirm other similar experimental and theoretical studies in the literature. The vitreous flow rates appearing in Figure 6 were validated by the experimental measurements of porcine vitreous flow in reference 3. The simulated results of 7500 cpm probes aspiration reflected similar vitreous performance of previous generation 5000 cpm probe where flow increased with increasing cut rate.[21,22] The simulated performance of BSS aspiration with 7500 cpm probes was also similar to published data: Diniz et al.[22] graphically demonstrated that BSS flow slightly decreased with increasing cut rate for 400 and 500 mm Hg vacuum: these differences were found to be significant ($P < 0.001$). Notice the difference between vitreous and BSS performance: vitreous flow decreased with increasing cut rate whereas BSS flow decreased. A published study postulated that the high cut rate may effectively reduce the viscosity of vitreous resulting in increased flow.[23]

The BSS flow rate profiles for the 50-50 duty cycle in Figure 3 closely resemble some of the profiles from the theoretical study of reference [24]. (The magnitude of flow is reversed and the units are different, because the model used in that study was only two-dimensional.) Although our study used a different numerical method for simulation, the flow model used for BSS flow was quite similar to that used in reference,[18] although the fluid viscosities were different.

The closest match is for the profiles in reference [24] at the highest cutting speeds and highest applied vacuum settings. Just after the inner shaft reaches the fully open position, the rate of flow into the vitrector temporarily decreases, and then increases steadily until the inner shaft begins moving towards the closed position. The cutting rate is too rapid to allow the flow rate to achieve a steady value while the port is fully opened. As the inner shaft moves towards the closed position, the flow rate at first decreases at a modest rate, and then rapidly returns to zero. All of these features are exhibited by the profiles for high cutting rate and high applied vacuum in reference.[24] The vitreous flow profiles are quite different from the flow profiles in reference [24], because a different flow model was used in our simulations for vitreous flow.

The findings of this simulation study further support the results of a clinical study reported in reference [25], which compared a variety of types of vitrectomy retinal surgical procedures. This study compared surgical outcomes of a group of 29 patients for which a low-speed (1500 cpm) 25-gauge vitrectomy system was used, versus a group of 27 patients for which an ultrahigh-speed (5000 cpm) 25-gauge vitrectomy system was used. Thirteen patients (21.7%) in the low-speed vitrector group had intraoperative iatrogenic retinal breaks, compared with only one patient (1.7%) in the ultrahigh speed vitrector group, presumably because of a reduction in retinal traction induced by the ultrahigh-speed vitrector. Surgeries performed using the ultrahigh-speed vitrector also took less time than when using the low-speed vitrector, consistent with the results of the current simulations.

Several simplifying assumptions were made in the construction of this model. The complicated and undefined geometry of the vitreous was reduced to a simple cylindrical shape at the point where it is entrained into the flow entering the vitrector port. It was assumed that under extension that this vitreous fiber bundle exhibits simple elastic properties, which is most likely a simplification of its actual mechanical response. Despite these simplifications, the model is capable of reproducing much of the experimental bench data. Future models may be improved to address these issues.

Conclusion

This simulation-based approach is currently being used for evaluating new cutter designs to enable even further reduced retinal traction, vitrectomy efficiency, and possible increased safety. The goal of vitrector probe design is to minimize retinal traction. Even though the performance of currently available vitrectors may be acceptable, there will always be room for improvement, since safety may improve as the applied retinal traction force approaches zero. Although this zero traction limit is practically unattainable, nevertheless there is benefit in comparative testing of the relative forces applied by probes of varying designs. To aid this design effort, this in silico method has been developed and qualified using laboratory data from a testing method that has been demonstrated previously to be able to distinguish between the performances of various vitrectors. This "virtual lab" method should enable rapid evaluation of the potential benefit of several design variations to select for successful designs, reducing the number of physical prototypes that would need to be fabricated and tested.

Acknowledgments

The authors are indebted to Russ Finlay of Alcon Surgical Sales Training for his careful review and suggestions, and to Hyo Won Choi of Data Science and Digital Solutions for his careful technical review.

Portions of this article were included in a poster presented at the Biomedical Engineering Society annual meeting held in Phoenix, Arizona, October 2017.

Disclosure: **P.J. Missel,** Alcon (E); **Y. Ma,** Alcon (E); **B.W. McDonell,** Alcon (E); **D. Shahmirzadi,** Alcon (E); **D.J.K. Abulon,** Alcon (E); **R. Sarangapani,** Alcon (E)

References

1. Rossi T, Querzoli G, Angelini G, et al. Fluid dynamics of vitrectomy probes. *Retina*. 2014;34:558–567.
2. Abulon DJK, Buboltz DC. Performance comparison of high speed dual-pneumatic vitrectomy cutters during simulated vitrectomy with balanced salt solution. *Trans Vis Sci Tech*. 2015;4(1):6.
3. Abulon DJK, Buboltz DC. Porcine vitreous flow behavior during high-speed vitrectomy up to 7500 cuts per minute. *Trans Vis Sci Tech*. 2016;5(1):7.
4. Abulon DJK. Vitreous flow rates through dual pneumatic cutters: effects of duty cycle and cut rate. *Clin Ophthalmol*. 2015;9:253.
5. Rizzo S, Polizzi S, Barca F, et al. Comparative study of 27-gauge versus 25-gauge

vitrectomy for the treatment of primary rhegmatogenous retinal detachment. *Hindawi J Ophthalmol*. 2017;2017:6384985.
6. Teixeira A, Chong L, Matsuoka N, et al. Novel Method to Quantify Traction in a Vitrectomy Procedure. *Br J Ophthalmol*. 2010;94:1226–1229.
7. Dugel PU, Zho J, Abulon DJK, et al. Tissue attraction associated with 20-gauge, 23-gauge, and enhanced 25-gauge dual-pneumatic vitrectomy probes. *Retina*. 2012;32:1761–1766.
8. Dugel PU, Abulon DJK, Dimalanta R. Comparison of attraction capabilities associated with high-speed, dual-pneumatic vitrectomy probes. *Retina*. 2015;35:915–920.
9. Kashani PS. Biomechanics of vitreous gel [dissertation] [Los Angeles (CA)] University of California, Los Angeles 2012, 126 p.
10. Dogramaci M, Lee EJ, Williamson TH. The incidence and the risk factors for iatrogenic retinal breaks during pars plana vitrectomy. *Eye*. 2012;26:718–722.
11. Landau LD, Lifshitz EM. Theory of elasticity, vol. 7. *Course of Theoretical Physics* (2nd Ed.) Pergamon: Oxford, 1970, p. 13.
12. Steel DHW, Charles S. Vitrectomy fluidics. *Ophthalmologica*. 2011;226(suppl 1):27–35.
13. Teixeira A, Chong LP, Matsuoka N, et al . Vitreoretinal traction created by conventional cutters during vitrectomy. *Ophthalmol*. 2010;117:1387–1392.
14. Rossi T, Querzoli G, Angelini G, et al . Instantaneous flow rate of vitreous cutter probes. *IOVS*. 2014;55:8289–8294.
15. Silva AF, Alves MA, Oliveira MSN. Rheological behaviour of viteous humour. *Rheol Acta*. 2017;56:377–386.
16. Yang L, van der Werf KO, Fitié CFC, et al. Mechanical properties of native and cross-linked type I collagen fibrils. *Biophys J*. 2008;94:2204–2211.
17. Chen EJ, Novakofski J, Jenkins WK, et al. Youn'gs modulus measurements of soft tissues with application to elasticity imaging. *IEEE Trans Ultrason Ferroelect Freq Cont*. 1996;43:191–194.
18. Fung YC. *Biomechanics: mechanical properties of living tissues*. New York: Springer-Verlag, 1981.
19. Silver FH, Bradica G, Tria A. Elastic energy storage in human articular cartilage: estimation of the elastic modulus for type II collagen and changes associated with osteoarthritis. *Matrix Biol*. 2002;21:129–137.
20. Moore SM, McMahon PJ, Debski RE. Bidirectional mechanical properties of the axillary pouch of the glenohumeral capsule: Implications for modeling and surgical repair. *J. Biomech Eng Trans ASME*. 2004;126:284–288.
21. Ribeiro RM, Teixeira AG, Diniz B, Fernandes R, Zhong Y, Kerns R, Humayun MS. Performance analysis of ultrahigh-speed vitreous cutter system. *Retina*. 2013;33:928–932.
22. Diniz B, Fernandes RB, Ribeiro RM, et al . Analysis of a 23-gauge ultra high-speed cutter with duty cycle control. *Retina*. 2013;33:933–938.
23. Magalhaes O, Chong L, DeBoer C, et al . Vitreous dynamics. Vitreous flow analysis in the 20-, 23-, and 25-gauge cutters. *Retina*. 2008;28:236–241.
24. Juan T, Hubschman J-P, Eldredge JD. A computational study of the flow through a vitreous cutter. *J Biomech Eng Trans ASME*. 2010;132:121005.
25. Rizzo S, Genovesi-Ebert F, Belting C. Comparative study between a standard 25-gauge vitrectomy system and a new ultrahigh-speed 25-gauge system with duty cycle control in the treatment of various vitreoretinal diseases. *Retina*. 2011;31:2007–2013.

Appendix A: Transient CFD Simulations

Transient CFD analyses were performed to solve for the fluid flow within all three domains. Simulations for flow of buffered aqueous saline solution assumed a single-phase Navier-Stokes fluid having the properties of water at 37°C, with a fluid viscosity of 8.9×10^{-4} kg/m^{-1}/s^{-1}. The same vacuum levels were used as for the simulations of vitreous flow: 650 mm Hg for enhanced 27+- gauge probes and 300 mm Hg for 23-gauge probes (this latter vacuum level was used to match the setting used during the measurements for vitreous cutting in the bench experiment for the 23-gauge probes).

When simulating vitreous flow and cutting, the transient CFD analysis used an Eulerian-Eulerian two-phase model (the Fluent mixture model), the separate phases representing the mixture of uncut vitreous and aqueous fluid in Zone I and the chopped vitreous mixture in Zones II and III. The Fluent mixture model is used because we make the approximation that vitreous material flows as a fluid, and that once it is cut and is aspirated into the vitrector, it experiences a change in viscosity. The mixture model allows each phase comprising the mixture to be modeled with different fluid properties. The density of each phase was 1 g/cm^3. The viscosity of chopped vitreous was 0.004 kg/m^{-1}/s^{-1}, which appears to be the

limit observed at high cut rate and high shear rate.[9] The viscosity of uncut vitreous, adjusted to match the previously reported vitreous flow rates[3] was found to be 0.02 kg/m^{-1}/s^{-1}. Simulations were conducted using a negative pressure boundary condition on the top end of the inner cutter shaft corresponding to the aspiration pressure setting used in the in vitro experiment, whereas driving the moving mesh displacement using a velocity profile derived from the shaft motion measured experimentally for the appropriate gauge probe and settings for cut rate and duty cycle. A zero-pressure boundary condition was maintained on the exterior of Zone I. The computational mesh was comprised of ~1 million elements, and the time-step ranged from 2.5 to 5 μsec for a total time as required to complete five full cycles of shaft motion, which enabled the flow solution to achieve quasi steady-state. A few studies were conducted with varying spatial and time discretization to verify that the method was independent of both mesh and time resolution. CFD simulations typically took five days to complete five shaft motion cycles with 16 cores engaged. By applying the suction boundary condition corresponding to the console setting, we are neglecting any pressure drop that may occur in the portion of the flow circuit between where the pressure setting is applied and the end of the shaft.

Appendix B: Transient Structural Simulations

The volume flow rate f(t) from the CFD simulation during the fifth cutter motion cycle was used as an input to drive the transient structural simulation as follows. The accumulated volume flow of material into the cutter as a function of time v(t) was obtained by integrating f(t) and was converted into displacement d(t) applied to the end of the fiber bundle using the following equation:

$$d(t) = \frac{v(t)}{\left[\frac{A_p}{2}\right]\rho}$$

where A_p is the cutter port area (the factor 2 appears because the geometry only represents half of the model) and ρ is the ratio of the surface area of the circular cross-section of an equivalent aspirated cylinder divided by the port area. Port areas were 9.68 × 10^{-8} m^2 for 27+-gauge and 1.29 × 10^{-7}/m^2 for 23-gauge. Observation of slow-motion videos of a cutter engaged in cutting porcine vitreous in vitro showed that approximately 1 mm of vitreous fiber is drawn into the cutter in one cycle for 27+-gauge. Thus we assign the length of the equivalent aspirated cylinder to be 1 mm. Because the amount of volume aspirated in one cycle (at a cut rate of 2500 cpm) for the 27+- and 23-gauge vitrectors is 2.48 × 10^{-4} and 4.76 × 10^{-4} mLs, respectively, the area of a cylinder representing the volume cut/aspirated in one cycle is 0.248 and 0.476 mm^2, respectively. Thus the values of ρ used were 2.56 and 3.69 for the 27+- and 23-gauge vitrectors, respectively. The same values of ρ for a particular gauge were used for all values of cut rate and duty cycle.

The simulation calculated the reaction force at the other end of the bundle that was attached to the force sensor. The geometric domain was meshed with ~200,000 elements, and a few studies were conducted with varying mesh resolution to verify that simulation results would not change upon changing mesh resolution. FEA simulations typically took 40 minutes to complete engaging 16 cores in a distributed memory simulation. ANSYS software (version 17.1; ANSYS, Inc. Canonsburg, PA, USA) was used to perform simulations using a Lenovo P-900 workstation equipped with dual Intel E5-2687W v3 processors (3.10 GHz, 10 cores each) and 128 GB RAM.

Appendix C: Transition in Flow Rate During Vitrectomy Surgery

In the beginning of the surgical procedure, the vitreous compartment is filled with intact vitreous having viscosity η_V, and if the vitrectomy is complete, at the end it is filled with buffered saline solution having viscosity η_B. We seek a continuous smooth function that will allow the flow rate to transition from f_V at the beginning to f_B at the end of surgery, where f_V and f_B correspond to the flow rate of pure vitreous and pure buffered saline solution through the probe when it is engaged in the cutting/aspirating operation. Consistent with our election to use the Fluent mixture model to simulate the fluid behavior of the mixture of cut vitreous and buffer, we assume the buffered saline solution entering the vitreous compartment mixes uniformly with the contents so that the viscosity of the entire compartment is uniform and can be expressed in terms of the volume fraction ϕ of unaspirated vitreous as follows:

$$\eta(\phi) = \phi\eta_V + (1-\phi)\eta_B \qquad \text{(C-1)}$$

Furthermore it is assumed that the effect of the changing material properties of the vitreous compartment on the flow rate through the vitrector is mediated

via the change in viscosity in a manner analogous to Poiseuille's law for flow through a pipe, which states that at constant pressure the velocity of fluid flowing through a pipe is proportional to the inverse of the viscosity. Thus we choose to approximate the flow velocity using the following function:

$$f(\phi) = \frac{\gamma(\phi)}{\eta(\phi)}, \tag{C-2}$$

where $\gamma(\phi)$ is a function that enables $f(\varphi)$ to transition from the value of f_V when $\varphi = 1$ to the value of f_B when $\varphi = 0$. Equation (C-2) may be rewritten as:

$$\gamma(\phi) = f(\phi)\ \eta(\phi) \tag{C-3}$$

It is simplest to use a linear function of φ for γ as follows:

$$\gamma(\phi) = I + S\,\phi \tag{C-4}$$

where I and S denote intercept and slope. When $\phi = 0$, $f(\phi) = f_B$, from Eq. (C-1) $\eta(\phi) = \eta_B$, and using Equations (C-3) and (C-4), we find that $I = \eta_B f_B$. Substituting this result for I into Eq. (C-4), when $\phi = 1$, $f(\phi) = f_V$, from Equation (C-1) $\eta(\phi) = \eta_V$, from Equations (C-3) and (C-4), we find that $S = \eta_V f_V - \eta_B f_B$. Thus the expression for $f(\phi)$ is given by:

$$f(\phi) = \frac{\eta_B f_B + (\eta_V - \eta_B f_B)\,\phi}{\phi\eta_V + (1-\phi)\,\eta_B} \tag{C-5}$$

This expression was used in numerical procedure in which time was advanced in a fixed small increment. At time zero, ϕ and f are set to their initial values 1 and f_V, respectively, and the vitreous compartment was set to 5 mL. The amount of vitreous removed during each time step was the flow rate at that time step times the value of f corresponding to the volume fraction ϕ for that time step using Equation (C-5). A new value of ϕ was then calculated taking into account the new amount of vitreous material divided by the volume of the compartment. The amount of buffered saline solution removed was assumed to comprise the remaining volume removed, or $f\,(1-\phi)$ times the time increment. It was found that using a time increment of one second was more than sufficiently small to cause the calculation results from this method to be independent of the size of the time increment. Figure C.1 shows how the volume fraction ϕ and the flow rate f were calculated to vary with time for the case of 27+-gauge vitrectors operating continuously at a cut rate of 2500 cpm with a duty cycle of 50/50, operating at an applied suction pressure of 650 mm Hg.

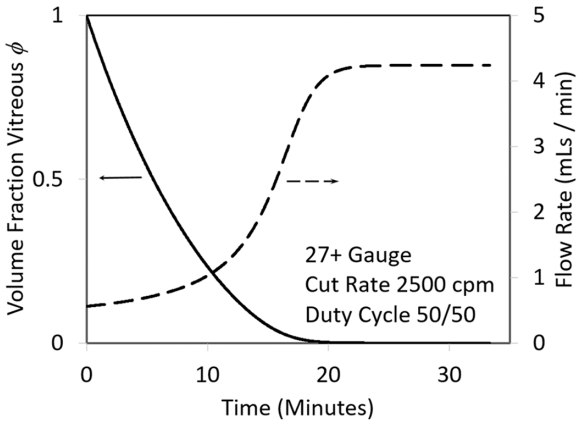

Figure C.1. Time dependence of vitreous volume fraction (*solid curve*) and flow rate of aspirated fluid (*dashed curve*) as predicted by the analytical approach described in Appendix C.